Interference patterns from post-collision interaction in below-threshold photoexcitation Auger processes

Xiao Wang[1] and F. Robicheaux[1,2,*]

[1]*Department of Physics and Astronomy, Purdue University, West Lafayette, Indiana 47907, USA*

[2]*Purdue Quantum Center, Purdue University, West Lafayette, Indiana 47907, USA*

(Received 25 May 2018; published 27 July 2018)

We focus on the post-collision interaction in Auger processes where the photoelectron energy is near or below the ionization threshold. Time-dependent quantum and classical calculations are performed. When the photoelectron is more deeply bound, interference patterns can be seen in the angular and photoelectron energy distributions. These interference patterns are visible in quantum calculations, but not in purely classical calculations. A semiclassical analysis using actions from two-path trajectories gives the relative locations of the interference maxima very close to those from the full quantum calculations.

DOI: 10.1103/PhysRevA.98.013421

I. INTRODUCTION

In Auger processes, the Coulomb interaction between the outgoing photoelectron and the Auger electron emitted later is known as the post-collision interaction (PCI) [1–7]. Typically, the energy of the Auger electron is much higher than the energy of the photoelectron, thus the fast Auger electron will pass the slow photoelectron a short time after the core decays. The effective charge of the ionic core that the photoelectron experiences suddenly changes from $+1$ to $+2$. The energy and angular momentum exchange between the two electrons can happen in the PCI due to the repulsive Coulomb interaction between them, and, in some cases, the ionized photoelectron can be recaptured to bound states with different energies or angular momenta [8–13].

The PCI has been extensively studied both theoretically and experimentally in the past few decades. Several early semiclassical theories considered extreme cases, where the energy of one electron is much greater than the other, like the Barker-Berry model [14], the Niehaus formula [15], and other derivations [6,16,17]. Later, many stationary quantal theories were developed, including those in Refs. [3–5,18,19], which gave similar PCI energy shifts but in a wider range of two electron energies. Detailed analyses of the angular momentum exchange in PCI can be found in Refs. [20–23]. Several time-dependent studies of PCI were developed in recent years [22,24–28]. Experimentally, the effect of PCI in a near-threshold photoionization has also been widely studied [7–13,29–32], while several studies mainly focused on angular correlation in the double continuum [33,34]

When the incident photon energy is much below the ionization threshold for an inner-shell electron, researchers study the resonant Auger process where the photon can excite an inner-shell electron to an excited bound state above the valence shell. There are also many studies of the resonant Auger process which has been thoroughly reviewed [2]. Intuitively thinking, with a high density of states, the PCI with slightly below-threshold photoexcitation and slightly above-threshold photoionization should behave similarly. However, our calculations show differences in the angular and photoelectron energy distributions (PED). This is partly due to the fact that a highly excited bound electron will return after it reaches its outer turning point, but a positive energy electron will not. Thus, the outgoing fast Auger electron could meet the photoelectron in a shorter distance and an earlier time, and the interaction between the two electrons would be stronger.

For the PED in an above-threshold photoionization, angular correlations have been investigated in experiments found in Refs. [35–37], and in the theories contained in Refs. [22,28,33,34,38]. There have not been studies focused on the PED in below-threshold photoexcitations, where the photoelectron gains enough energy to be ionized due to the PCI. In this paper, we focus on the PED in below-threshold photoexcitation Auger process at different initial conditions, including photoelectron energy and Auger width. Interference patterns can be found in the PED. Properties of the interference patterns in PED at different initial conditions are studied, and also analyzed from a semiclassical approach. Both a quantum method, by solving two-electron time-dependent Schrödinger equations, and a classical method, by solving Hamilton's equations, are used in this paper to study the PCI effect across the ionization thresholds. Our method is based on Refs. [22,38–40], with extensions to negative photoelectron energies.

This paper is structured as follows. In Sec. II, a model of the Auger process and the quantum and classical numerical methods used in this paper are briefly introduced. In Sec. III, the results from both quantum and classical calculations are presented and compared. Also in Sec. III, the PED is studied for different photoelectron energies across the threshold, and for different Auger widths. Atomic units are used unless specified otherwise.

II. NUMERICAL METHODS

Instead of a full model considering all electrons in an atom, we consider only the photoelectron and the Auger

*robichf@purdue.edu

electron in our calculations. This approximation can be made because significant interactions between the two electrons mostly happen outside the ionic core. Therefore, the detailed shell structure is less important and can be interpreted as a simple model potential.

Additionally, we limit our calculations with total angular momentum L, as well as the initial angular momentum for each electron, being 0. This approximation can greatly reduce the number of coupled angular channels in the calculation. From Ref. [21] and our analyses in Sec. III, the angular momentum exchange between the two electrons are fairly weak. Also, since the electron-electron interactions mostly occur far from the ionic core, we assume that the results from the $L = 0$ approximation will not significantly misinterpret the essence of energy and angular momentum exchange in the PCI. For the cases with nonzero angular momentum, brief discussions are given at the end of Sec. III C.

A. Quantum methods

The dynamics of the emitted photoelectron before the Auger core decays can be described by the following time-independent inhomogeneous Schrödinger equation [22,38]:

$$\left(E_1 + i\frac{\Gamma_c}{2} - H_a\right)F_1(\mathbf{r_1}) = D\phi_g(\mathbf{r_1}), \tag{1}$$

where $E_1 = E - E_c$ is the incident photon energy minus binding energy of the Auger core, and E_1 is also the photoelectron energy above the ionization threshold. Γ_c is the Auger core width, and $H_a = \mathbf{p_1}^2/2 + V(\mathbf{r_1})$ is the Hamiltonian for the photoelectron. The imaginary $i\Gamma_c/2$ is applied to the Auger core energy E_c to calculate the wave function of the photoelectron before the Auger core decays. While the authors of Ref. [38] gave the mathematical reason for this positive imaginary term, the qualitative reason is that it leads to a finite spatial extent for $F_1(\mathbf{r_1})$ even when E_1 is positive, which reflects that the part of the wave function representing a photoelectron with **no** Auger electron should have a finite extent in r_1. The $D\phi_g$ is the dipole operator acting on the ground-state wave function of the inner-shell photoelectron. With the approximations we proposed at the beginning of this section, the $D\phi_g$ can be chosen as any short range function as long as the following conditions are met: (1) it is not orthogonal to the continuum wave function of the photoelectron F_1 and, (2) it has the correct angular momentum. For the potentials in our problem, we may use a model potential that has an asymptotic form of $-Z/r$ as $r \to \infty$:

$$V(r) = -\frac{Z + (Z_t - Z)e^{-r/r_a}}{r}, \tag{2}$$

where Z_t, r_a are adjustable parameters that represent the properties of the model potential or, different atomic structures. We may also use a Coulomb potential with $V(r) = -Z/r$ as a simplified model. Here in H_a, we have $Z = 1$ in the potential for the photoelectron.

After the Auger core decays, the dynamics of the two electron system can be described by the following time-dependent Schrödinger equation [22,38]

$$\left(i\frac{\partial}{\partial t} + E_1 + E_2 - H\right)\Lambda(\mathbf{r_1}, \mathbf{r_2}, t) = S(t)F_1(\mathbf{r_1})F_2(\mathbf{r_2}), \tag{3}$$

$$H = \frac{\mathbf{p_1}^2}{2} + \frac{\mathbf{p_2}^2}{2} + V(\mathbf{r_1}) + V(\mathbf{r_2}) - \frac{1}{|\mathbf{r_1} - \mathbf{r_2}|}, \tag{4}$$

where H is the full two-electron Hamiltonian with $Z = 2$ in the potentials for both electrons. E_2 is the energy of the Auger electron above the ionization threshold. F_2 is a short-range function that represents the source term for the Auger electron, and it is not orthogonal to the Coulomb eigenstate at E_2. $S(t)$ is a step-like function that acts as the source term for the Auger decays, and we choose $S(t) = 1/(1 + \exp[10\{1 - 5t/t_f\}])$ in our calculations [38], where t_f is the final time of the calculation that all physical quantities are stable.

The whole two-electron wave function $\Lambda(\mathbf{r_1}, \mathbf{r_2}, t)$ is represented on a three-dimensional mesh

$$\Lambda(\mathbf{r_1}, \mathbf{r_2}, t) = \sum_{l=0}^{L_{\max}} (-1)^l R_l(r_1, r_2, t) Y_{l0}(\cos\theta_{12}), \tag{5}$$

where the $Y_{l0}(\cos\theta_{12})$ are the spherical harmonics on the relative angle between $\mathbf{r_1}$, $\mathbf{r_2}$, and the phase factor follows the convention in [28,41]. $L_{\max}$ is the maximum number of coupled angular channels in the calculations, chosen to give converged results. In the radial dimension, a square root mesh is used which provides more grid points near the origin. For the time propagation of the wave function, the split operator method and the implicit Crank-Nicolson method are used. When dealing with the $1/r_{12}$ operator, the discrete variable representation is used for the coupling between different angular momenta. Further details of the numerical calculations can be found in Ref. [39].

It can be seen from Eq. (3) that the two-electron wave function Λ has an increasing probability from the source term for Auger decay. At the final time of the calculation, physical quantities should be extracted as their time derivatives normalized by the probability increasing rate of Λ [42]. This can be understood that the probability to find the system in a given channel is equal to the *rate* that electrons go into the channel divided by the norm increasing *rate* of the whole two-electron wave function. For example, the probability that the two electrons having energy ϵ_1, ϵ_2 and angular momentum l_1, l_2, respectively, can be calculated as

$$P(\epsilon_1, \epsilon_2, l_1, l_2) = \frac{\frac{d}{dt}|\langle f_{\epsilon_1 l_1} f_{\epsilon_2 l_2}|\Lambda(t)\rangle|^2}{\frac{d}{dt}|\langle\Lambda(t)|\Lambda(t)\rangle|^2}, \tag{6}$$

where the Coulomb wave function $f_{\epsilon l}$ should be energy normalized for a continuum eigenstate, and unity normalized for a bound eigenstate.

B. Classical methods

It has been shown in many previous studies, e.g., Ref. [43], that a highly excited Rydberg electron or a continuum electron often can be approximated as a classical particle. We can use the much faster and more efficient classical-trajectory Monte Carlo

method to understand the system in a totally different approach. The classical method can also give intuitive interpretations to the PCI.

In every Monte Carlo trajectory, a photoelectron is emitted near the origin at $t_1 = 0$ [22]. The energy of the photoelectron satisfies a normal distribution centered at E_1 with standard deviation $\sigma = \Gamma_c/2\sqrt{2\ln 2}$. The initial angular momentum and angular distribution should satisfy those given in $D\phi_g(\mathbf{r_1})$. After a delay time of t_2, which satisfies an exponential distribution $\Gamma_c \exp(-\Gamma_c t)$, the Auger electron is emitted near the origin. The energy of the Auger electron is the difference of the photoelectron energy from the total incident photon energy. The initial angular momentum and angular distribution of the Auger electron are the same as those from $F_2(\mathbf{r_2})$. With these initial conditions, we can propagate the classical system using Hamilton's equations, and extract the physical quantities as a statistical distribution at the final time of the calculation. Further details can be found in Refs. [22,39,40]

III. RESULTS AND DISCUSSIONS

In Sec. III A, we report results from calculations using quantum and classical methods to show the validity of these methods with model potentials and negative energy photoelectrons. In Sec. III B and Sec. III C, calculations are performed in pure Coulomb potentials, and we mainly focus on the quantum results of PED and the semiclassical interpretations. All calculations performed in this section have zero total angular momentum, and zero initial angular momentum for both electron.

A. Comparisons between quantum and classical methods

We first perform calculations using a model potential as given in Eq. (2) with $r_a = 1.0$, $Z_t = 6.0$. In this model potential with nuclear charge $Z = 1$, the quantum defects for Rydberg states with different angular momentum are approximately $\delta_s = 1.27$, $\delta_p = 0.97$, $\delta_d = 0.19$, $\delta_f = 0.008$. For $Z = 2$, the quantum defects are $\delta_s = 0.88$, $\delta_p = 0.70$, $\delta_d = 0.35$, $\delta_f = 0.06$. In the calculation, we have the Auger core width $\Gamma_c = 0.003$ a.u. ≈ 82 meV and Auger electron energy $E_2 = 2.0$ a.u. ≈ 54 eV. The photoelectron energy is set to be $E_1 = -6.0 \times 10^{-3}$ a.u., below the threshold, where the Rydberg spacing is much smaller than the Auger width. Also, for simplicity of the calculation, the initial angular momentum for both electrons is set to be zero.

The energy and state distributions for the photoelectron after PCI are plotted in Fig. 1, from both quantum and classical calculations. Since there is no quantization for a classical system, the classical energy distribution is a continuous function, and it has a similar distorted shape to those calculations for an above-threshold Auger process [21,22,28]. On the other hand, the quantum system is quantized and the photoelectron can only be in discrete eigenstates. The probabilities to find the photoelectron in different states are given in the figure. The overall envelope of the quantum state distribution qualitatively agrees with the classical energy distribution. Using the Niehaus formula [15], the maximum of the photoelectron energy distribution is located at -0.0157, while our classical calculation gives -0.0167. The initial energy $E_1 = -6.0 \times 10^{-3}$ a.u. is

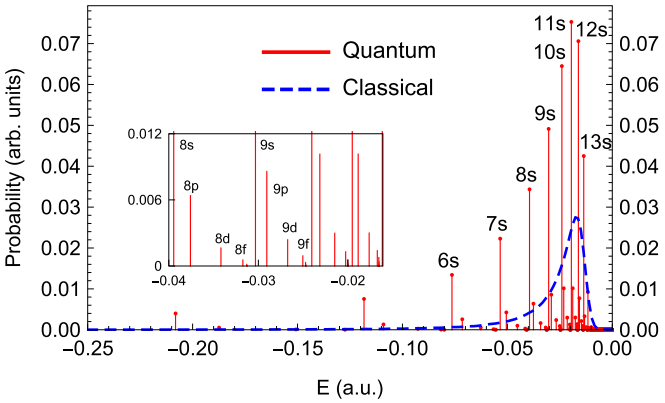

FIG. 1. Photoelectron energy distributions after PCI from both quantum and classical calculations. The initial photoelectron energy is $E_1 = -6.0 \times 10^{-3}$ a.u., below the threshold. Auger electron energy is $E_2 = 2.0$ a.u. above the threshold, and the Auger width is $\Gamma_c = 3.0 \times 10^{-3}$ a.u. The inset figure is a magnification of quantum results at high density of Rydberg state.

close to the resonant state of $10s$ of $Z = 1$. After the PCI, the photoelectron is shaken-up to those $11s$, $12s$, $13s$ states of $Z = 2$, although the photoelectron loses energy in the PCI. The ionization probabilities from both quantum and classical calculations are about 0.5%.

The authors of Refs. [20–23] discussed the angular momentum exchange and angular distribution between the two electrons due to the PCI. For our calculations of the angular momentum distributions, the ns peaks have much higher probabilities than other nonzero angular momentum peaks. Our quantum calculations show that about 82% of the photoelectron wave function after PCI is in s orbitals. We also count the probability that the classical angular momentum is within $0 \leqslant l < 1$, and the result is 78%. These calculations show that the angular momentum exchange during the PCI with these initial parameters is fairly weak but nontrivial, and most of the wave function tends to keep its initial angular momentum.

B. Photoelectron angular and energy distributions

To further study the energy and angular momentum exchange during the PCI for near-threshold photoionizations (or photoexcitations), we perform multiple quantum calculations at different photoelectron launch energies across the threshold. The following calculations are performed with Auger electron energy $E_2 = 2.0$ a.u. and Auger width $\Gamma_c = 0.003$ a.u. The photoelectron energies are varied. The initial angular momentum for both electrons are set to be zero to simplify the calculations. All of the following calculations are performed in a pure Coulomb potential. Although we do not show model potential calculations, they give very similar results.

In PCI with the photoelectron energy near the threshold, the vast majority of the photoelectron wave function loses energy due to the change of nuclear charge from $+1$ to $+2$ when the Auger electron leaves the atom. However, when the outgoing angles of the two electrons are nearly the same, the early ejected photoelectron may be strongly repelled by the Auger electron. As a result, the photoelectron gains energy, and its momentum direction is also changed from its initial

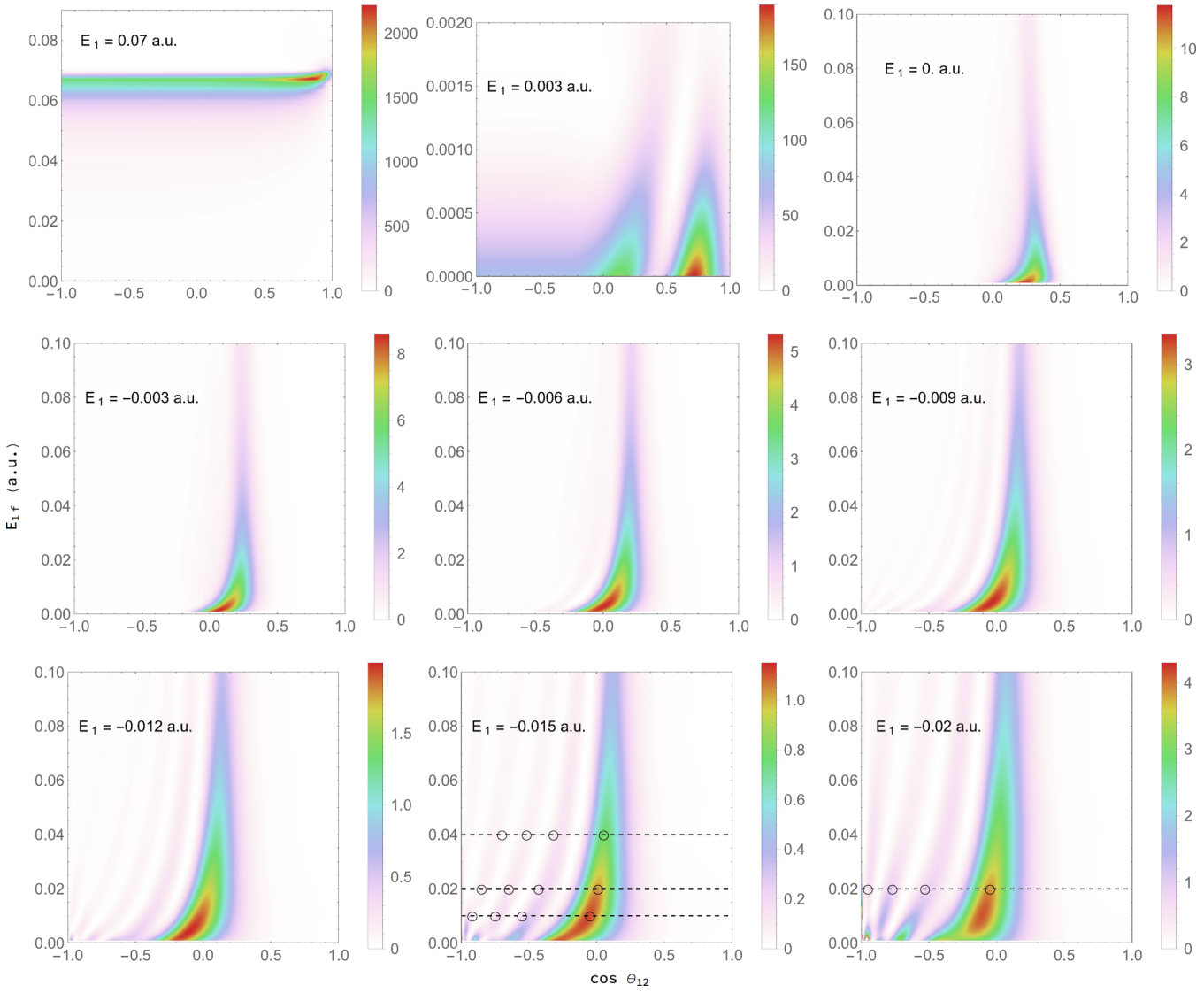

FIG. 2. Quantum results of the angular ($\cos\theta_{12}$) and photoelectron energy (E_{1f}) distributions (PED) at different initial photoelectron energy E_1. The initial Auger electron energy is $E_2 = 2.0$ a.u., and Auger width is $\Gamma_c = 0.003$ a.u. The photoelectron energy E_1 is given at the top left of each subfigure. Note that, the E_{1f} and PED scales are different in different subfigures. All calculations are performed at the same initial intensity in the source terms. Among different subfigures, the PED number is proportional to their absolute count of detections due to the same initial photon intensities. The dashed horizontal lines in the subfigures of $E_1 = -0.015$ and -0.02 a.u. are plotted at $E_{1f} = 0.01$, 0.02, and 0.04 a.u. The small circles are the corresponding classical maxima presented later in the text.

outgoing direction. Therefore, we study the correlation of the photoelectron energy (E_{1f}) versus the relative angle between momentum of the two outgoing electrons (θ_{12}). Both values are achieved at a long final time when they are already stable. We focus on the angular and photoelectron energy distributions (PED) of the wave functions in the double continuum.

In Fig. 2, the PED from *quantum* calculations are plotted for different initial photoelectron energies E_1. When E_1 is well above the threshold at 0.07 a.u., most of the photoelectron wave functions have a lower energy but still remains ionized, and the angular distribution is nearly spherically symmetric other than for those $\cos\theta_{12}$ near 1 [35,38]. When E_1 is slightly above the threshold at 0.003 a.u., two local maxima can be found in the figure. The right peak originates from those positive energy, outgoing photoelectrons being closely passed by a late emitted fast Auger electron at a large distance away from the nucleus. The photoelectron is then pushed aside to a slightly larger angle, and still remains in the continuum. Photoelectrons in the left peak near $\cos\theta_{12} = 0$ are due to the repulsion from an early emitted Auger electron just after the photoionization. The strong repulsion may directly push the photoelectron to a much larger angle than the previous scenario. Detailed analyses can be found in Ref. [22].

As the photoelectron energy E_1 decreases and goes below the threshold, the absolute value of the PED also decreases. This is partly due to the fact that, as E_1 gets lower, the Rydberg spacings become greater than the Auger width, and the initial photoabsorptions at nonresonant energies are much weaker. The abnormal increase in the PED for $E_1 = -0.02$ a.u. is because -0.02 a.u. is an eigenenergy of a pure Coulomb potential with $n = 5$ and $Z = 1$. With the same intensity in the initial source terms, the resonant photoabsorption at -0.02 a.u.

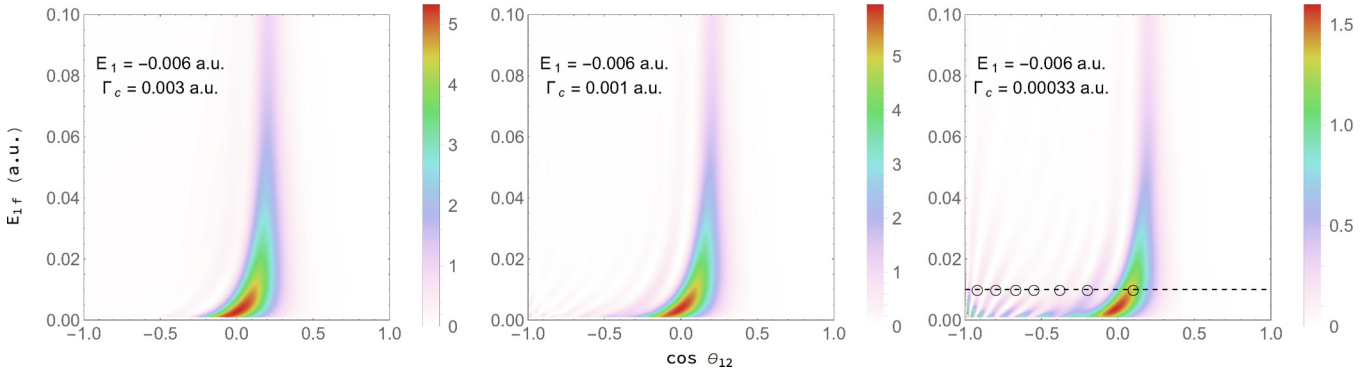

FIG. 3. Quantum results of the PED at $E_1 = -0.006$ a.u., and different Γ_c. The Γ_c is given at the top left of each subfigure. The initial Auger electron energy is $E_2 = 2.0$ a.u. Other properties are the same as those given in the caption of Fig. 2. The dashed horizontal line in the subfigure of $\Gamma_c = 3.3 \times 10^{-4}$ a.u. is plotted at $E_{1f} = 0.01$ a.u. The small circles are the corresponding classical maxima presented later in the text.

causes higher counts in the double continuum. The ionization probabilities barely decrease to 0.4% for $E_1 = -0.02$ a.u., comparing to the 0.5% for $E_1 = -0.006$ a.u.

Comparing the subfigures for $E_1 = 0.003$ a.u. and $E_1 = 0$ a.u., the "right" peak disappears, and the "left" peak grows. This indicates a nearly zero probability for an outgoing photoelectron being closely scattered by an Auger electron *at a large distance* and still remain positive energy, as those scenarios described earlier for the $E_1 = 0.003$ a.u. Another interesting feature in Fig. 2 is that, as the E_1 decreases, interference patterns start to appear in the distributions. However, those interference patterns do not exist in classical calculations with the same parameters, which indicates that those patterns are quantum effects. The subfigure for $E_1 = -0.02$ a.u. also illustrates that resonance in the initial photoelectron excitation has no significant effect in those final interference patterns.

To study the interference patterns at different initial conditions, we perform several quantum calculations with the same E_1 at -0.006 a.u. but different Γ_c. The resulting PED can be seen in Fig. 3. The interference pattern is barely visible at $\Gamma_c = 0.003$ a.u., but is very clear at $\Gamma_c = 3.3 \times 10^{-4}$ a.u. A smaller Γ_c gives well-resolved energy spectrum in the photoabsorption, and that leads to better-resolved interference patterns in the PED.

Another feature is that the oscillations in the interference pattern are much faster than that of $E_1 = -0.015$ a.u. or -0.02 a.u. This can be interpreted using our semiclassical approach introduced in the next subsection.

Further estimations and numerical calculations show that, when the photoelectron energy satisfies $E_1 < -0.5\,\Gamma_c^{2/3}$, the interference pattern starts to be visible. This is also the energy, E_1, that the Rydberg spacings $\sim n^{-3}$ equals the Auger width, and states with different principal quantum number n are resolved by the photoexcitation photon and the Auger decay rate.

C. Semiclassical interpretations of the interference patterns in PED

Interference in quantum systems often results from two paths leading to the same final state. Since the quantum and classical calculations give similar results for a below-threshold photoexcitation Auger process as presented in Sec. III A, multiple classical calculations are performed to qualitatively study the quantum interference patterns. We trace back those classical trajectories that give specific E_{1f} and $\cos\theta_{12}$ at the final time, and study their spatial trajectories and initial launch variables. With fixed initial energies for the photoelectron and Auger electron, only two variables may affect the final values of E_{1f} and $\cos\theta_{12}$: the Auger decay time t_2 after the photoelectron excitation, and the initial launch angle difference ω between the two electrons.

In classical trajectories, there exists a mapping from the initial pair $(\cos\omega,\ t_2)$ to the final pair $(\cos\theta_{12},\ E_{1f})$. For example, when $E_1 = -0.015$ a.u., $E_{1f} = 0.02$ a.u., the function of $\cos\theta_{12} \sim (\cos\omega,\ t_2)$ is given in Fig. 4. Note that,

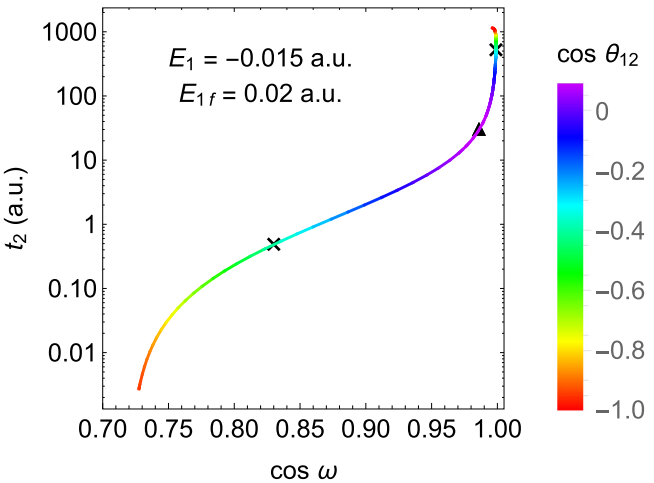

FIG. 4. The relation of t_2 versus $\cos\omega$ with a fixed $E_{1f} = 0.02$ a.u. The $\cos\theta_{12}$ value, which is the angle difference in the asymptotic momentum of the two continuum electrons, is marked with different colors. The ω is the angle difference between the launch directions of the two electrons, and t_2 is the time of Auger decay after launch of the photoelectron. Two X's are plotted at $(0.83, 0.45)$ and $(0.9989, 630)$, which both give $\cos\theta_{12} = -0.4$. The triangle is plotted at $(0.987, 32.8)$, which is the transition point that distinguishes the two paths, and is also the initial condition to achieve the classically maximum allowed $\cos\theta_{12} = 0.108$.

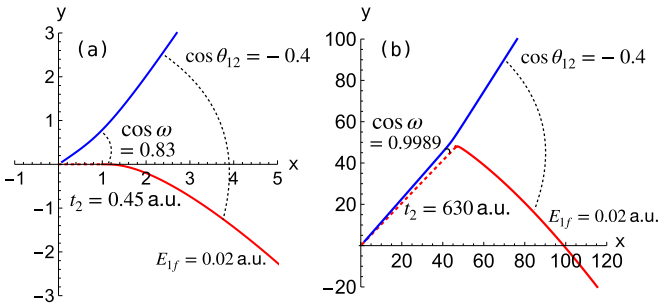

FIG. 5. Illustrations for the two classical trajectories with final angle $\cos\theta_{12} = -0.4$ and photoelectron energy $E_{1f} = 0.02$ a.u. The nucleus is located at the origin. The red and blue lines are trajectories for photoelectron and Auger electron, respectively. The dashed red lines are photoelectron trajectories before the Auger decay. The figure (a) refers to an early Auger decay, and the figure (b) refers to a late Auger decay.

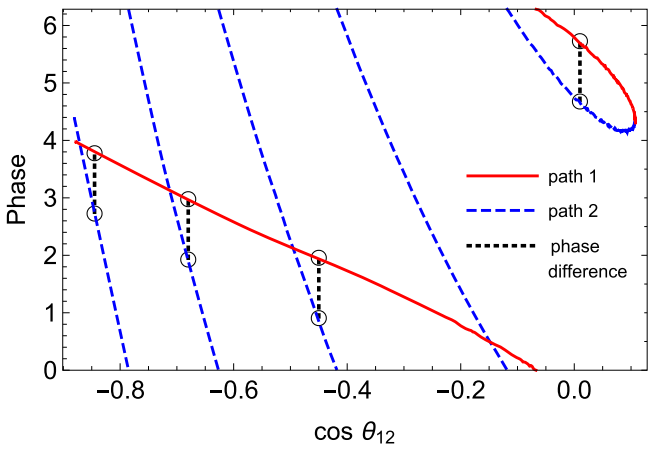

FIG. 6. The classical phases from the two paths versus different final value of $\cos\theta_{12}$, at the same final energy of $E_{1f} = 0.02$ a.u. The action difference reaches a local maximum around $\cos\theta_{12} = 0$, and $\delta S = 1.05$, which is plotted in black dotted line. The $(\cos\theta_{12}, E_{1f}) = (0, 0.02)$ is a constructive interference point as presented in Fig. 2. All other three black dotted lines represent the same phase differences $\delta\varphi = 1.05$, and are plotted at $\cos\theta_{12} = -0.45, -0.67, -0.85$, respectively.

for initial angle $\cos\omega < 0.7$, it is nearly impossible for the photoelectron to gain enough energy and become ionized. On this curve, to achieve $\cos\theta_{12} = -0.4$, which is close to a quantum constructive interference region in Fig. 2, there are two classical trajectories with totally different initial values. Illustrations for the two trajectories are given in Fig. 5. The first trajectory has $\cos\omega = 0.83$, $t_2 = 0.45$ a.u., and the second trajectory has $\cos\omega = 0.9989$, $t_2 = 630$ a.u. In the first trajectory, the photoelectron is directly pushed out by the early emitted Auger electron. For the second trajectory, we have $t_2 > 0.5\,T_{\mathrm{Rydl}} \approx 604$ a.u. The Auger decay happens when the photoelectron is just starting to return to the nucleus, and the emitted angle of the Auger electron is very close to that of photoelectron. The returning photoelectron is then scattered by the outgoing Auger electron, gains energy, and gets ionized from the atom in a different direction from its initial launch direction. Since there are two totally different paths that can reach the same final region in the double continuum, quantum interferences exist, and interference patterns can be found in the PED figure.

We also use a semiclassical idea to analyze the quantum interference pattern as presented in Fig. 2. We consider the two classical paths that go to the same final region in $\cos\theta_{12}$ and E_{1f}, and accumulate their classical actions as the time integral of their respective Lagrangians from the launch of photoelectrons to a large fixed final time. For example, in the problem with $E_1 = -0.015$ a.u., $E_2 = 2.0$ a.u. and $\Gamma_c = 0.003$ a.u., we consider the thick horizontal dashed line of $E_{1f} = 0.02$ a.u. in the PED plot given in Fig. 2. The relation of $\cos\theta_{12}$ versus initial value $(\cos\omega,\ t_2)$ pairs are given in Fig. 4. Since the photoelectron is in a periodic Rydberg motion before Auger decay, we may only consider cases that the t_2 is less than one Rydberg period. For the first path with small t_2 and small $\cos\omega$, the $\cos\theta_{12}$ increases as $\cos\omega$ and t_2 increase until reaching the classically maximum allowed $\cos\theta_{12} = 0.108$ at this energy, where $\cos\omega = 0.987$ and $t_2 = 32.8$. Beyond this point, the $\cos\theta_{12}$ decreases as the t_2 increases, which gives the mapping of the second path. We then calculate the semiclassical actions S accumulated from the two paths, and δS as the action difference. The phases φ, which are the actions modulo 2π, versus $\cos\theta_{12}$ are given in Fig. 6. Comparing to the quantum results in Fig. 2, where the global maximum for $E_{1f} = 0.02$ a.u. is achieved at around $\cos\theta_{12} = 0$, the classical action difference $\delta S = 1.05$ can be found at this angle. We then find those classical paths having action differences $\delta S = 1.05 \pm k \cdot 2\pi$, where k is an integer. The classical paths with final angles of $\cos\theta_{12} = -0.45, -0.67$, and -0.85 have phase differences $\delta\varphi = 1.05$ modulo 2π, and these $\cos\theta_{12}$ values are approximately the same constructive interference angles as those presented in Fig. 2. Similarly, classical maxima are also calculated at several other E_{1f} values and different initial conditions, and their locations can be found in Fig. 2 and Fig. 3.

In Fig. 3, the locations of interference maxima do not change with Auger width Γ_c, and the interference patterns are better resolved when the Γ_c gets smaller. This can be understood that the Γ_c only controls the distributions of the Auger decay time t_2, but not the actual electronic dynamics. With a smaller Γ_c, the t_2 has a higher probability to be a large value, which could result in more trajectories of those extreme conditions in $\cos\theta_{12}$ or E_{1f}. On the other hand, the interference intensities oscillate much faster in Fig. 3 with $E_1 = -0.006$ a.u. than that in Fig. 2 with $E_1 = -0.015$ a.u. The fast change in the relative interference phase comes from the rapid increase in the semiclassical action in the second path, where the returning photoelectron is scattered by the fast outgoing Auger electron. In the second path, the Auger electron is emitted a long time after excitation of the photoelectron. Considering the Bohr-Sommerfeld quantization condition, the photoelectron accumulates more actions with a higher initial energy. Thus, the semiclassical phases would be more sensitive to the launch time t_2 and final angle $\cos\theta_{12}$.

Further studies of this model can be extended to nonzero initial angular momentum. We know that the interference patterns are constructed from two paths, and one crucial path

is at small ω and large t_2. For nonzero angular momentum, the initial angular distributions of the photoelectron and Auger electron are polarized. If they have the same polarization angle, there will be a higher chance that the initial angle difference ω is a small value, and the interference patterns would be brighter and easier to observe in experiment. Furthermore, since our calculations are performed with zero angular momentum using pure Coulomb potential or simple model potential, study of nonzero angular momentum in a sophisticated model potential could be an interesting topic. A nonnegligible ionic core could twist the motion of electrons at small distance near the nucleus, thus the dynamics of the first path would be affected. The exact interference patterns might be different in different atoms.

IV. CONCLUSION

In this paper, we perform quantum calculations and classical calculations to numerically study the Auger process and the post-collision interaction. Both methods are time-dependent calculations, which can help us better understand the time-resolved dynamics of the Auger process. We mainly focused on those photoexcitation and photoionization scenarios in which the excited (or ionized) photoelectron energy is near the ionization threshold. An initial calculation demonstrated the effectiveness of our classical method when describing a quantum model with negative photoelectron energy and model potential. The numerical results showed that the angular momentum exchange during the post-collision interaction is fairly weak [20–23]. To further study the interaction between the two electrons during the post-collision interaction, we focused on the correlation of angular and photoelectron energy distribution. We decreased the initial energy of the photoelectron, and checked the PED at different initial photoelectron energies and Auger core widths. Interestingly, when the initial energy of the photoelectron is low enough, interference patterns can be found in the PED. We studied the mappings between initial values of launch time and angles and final values of energies and angles in the interference region. We find that there are two paths with different initial conditions that can contribute to the same final region in the double continuum. We used a semiclassical treatment to calculate the classical actions as the time integral of the Lagrangian of the system, and calculated the phase difference of the two paths. Along a given line in the PED correlation figure, our semiclassical treatment gave the relative locations of the interference maxima, which are nearly the same as those from quantum calculations. Finally, we briefly discussed our model with nonzero initial angular momentum, and proposed further studies on those interference patterns in different atomic systems.

ACKNOWLEDGMENTS

The authors would like to thank Prof. C. H. Greene for helpful discussions. This material is based upon work supported by the US Department of Energy, Office of Science, Basic Energy Sciences, under Award No. DE-SC0012193. This research was supported, in part, through computational resources provided by Information Technology at Purdue University, West Lafayette, Indiana.

[1] G. C. King, F. H. Read, and R. C. Bradford, J. Phys. B **8**, 2210 (1975).
[2] G. B. Armen, H. Aksela, T. Åberg, and S. Aksela, J. Phys. B **33**, R49 (2000).
[3] M. U. Kuchiev and S. A. Shenerman, Soviet Phys. Uspekhi **32**, 569 (1989).
[4] M. Y. Kuchiev and S. A. Sheinerman, J. Phys. B **21**, 2027 (1988).
[5] M. Y. Kuchiev and S. A. Sheinerman, J. Phys. B **18**, L551 (1985).
[6] F. H. Read, Radiat. Res. **64**, 23 (1975).
[7] Y. Lu, W. C. Stolte, and J. A. R. Samson, Phys. Rev. A **58**, 2828 (1998).
[8] U. Hergenhahn, A. D. Fanis, G. Prümper, A. K. Kazansky, N. M. Kabachnik, and K. Ueda, J. Phys. B **38**, 2843 (2005).
[9] S. Kosugi, M. Iizawa, Y. Kawarai, Y. Kuriyama, A. L. D. Kilcoyne, F. Koike, N. Kuze, D. S. Slaughter, and Y. Azuma, J. Phys. B **48**, 115003 (2015).
[10] R. Hentges, N. Müller, J. Viefhaus, U. Heinzmann, and U. Becker, J. Phys. B **37**, L267 (2004).
[11] J. A. R. Samson, Y. Lu, and W. C. Stolte, Phys. Rev. A **56**, R2530(R) (1997).
[12] J. A. R. Samson, W. C. Stolte, Z. X. He, J. N. Cutler, and D. Hansen, Phys. Rev. A **54**, 2099 (1996).
[13] W. Eberhardt, S. Bernstorff, H. W. Jochims, S. B. Whitfield, and B. Crasemann, Phys. Rev. A **38**, 3808 (1988).
[14] R. B. Barker and H. W. Berry, Phys. Rev. **151**, 14 (1966).
[15] A. Niehaus, J. Phys. B **10**, 1845 (1977).
[16] G. Nienhuis and H. G. M. Heideman, J. Phys. B **9**, 2053 (1976).
[17] J. Mizuno, T. Ishihara, and T. Watanabe, J. Phys. B **18**, 1241 (1985).
[18] G. B. Armen, J. Tulkki, T. Aberg, and B. Crasemann, Phys. Rev. A **36**, 5606 (1987).
[19] A. Russek and W. Mehlhorn, J. Phys. B **19**, 911 (1986).
[20] A. Niehaus and C. J. Zwakhals, J. Phys. B **16**, L135 (1983).
[21] L. Gerchikov, R. Guillemin, M. Simon, and S. Sheinerman, Phys. Rev. A **95**, 063425 (2017).
[22] Q. Wang and S. D. Loch, Phys. Rev. A **91**, 053416 (2015).
[23] L. Gerchikov and S. Sheinerman, J. Phys. B **51**, 065201 (2018).
[24] A. K. Kazansky and N. M. Kabachnik, Phys. Rev. A **72**, 052714 (2005).
[25] U. Hergenhahn, A. De Fanis, G. Prümper, A. K. Kazansky, N. M. Kabachnik, and K. Ueda, Phys. Rev. A **73**, 022709 (2006).
[26] A. K. Kazansky and N. M. Kabachnik, Phys. Rev. A **73**, 062712 (2006).
[27] A. K. Kazansky, I. P. Sazhina, and N. M. Kabachnik, J. Phys. B **42**, 245601 (2009).
[28] Q. Wang, S. Sheinerman, and F. Robicheaux, J. Phys. B **47**, 215003 (2014).
[29] H. Aksela, M. Kivilompolo, E. Nõmmiste, and S. Aksela, Phys. Rev. Lett. **79**, 4970 (1997).
[30] P. Lablanquie, S. Sheinerman, F. Penent, T. Aoto, Y. Hikosaka, and K. Ito, J. Phys. B **38**, L9 (2005).
[31] F. Penent, S. Sheinerman, L. Andric, P. Lablanquie, J. Palaudoux, U. Becker, M. Braune, J. Viefhaus, and J. H. D. Eland, J. Phys. B **41**, 045002 (2008).

[32] R. Guillemin, S. Sheinerman, R. Püttner, T. Marchenko, G. Goldsztejn, L. Journel, R. K. Kushawaha, D. Céolin, M. N. Piancastelli, and M. Simon, Phys. Rev. A **92**, 012503 (2015).
[33] S. A. Sheinerman and V. Schmidt, J. Phys. B **30**, 1677 (1997).
[34] P. van der Straten, R. Morgenstern, and A. Niehaus, Z. Phys. D **8**, 35 (1988).
[35] A. L. Landers, F. Robicheaux, T. Jahnke, M. Schöffler, T. Osipov, J. Titze, S. Y. Lee, H. Adaniya, M. Hertlein, P. Ranitovic, I. Bocharova, D. Akoury, A. Bhandary, T. Weber, M. H. Prior, C. L. Cocke, R. Dörner, and A. Belkacem, Phys. Rev. Lett. **102**, 223001 (2009).
[36] F. P. Sturm, M. Schöffler, S. Lee, T. Osipov, N. Neumann, H.-K. Kim, S. Kirschner, B. Rudek, J. B. Williams, J. D. Daughhetee, C. L. Cocke, K. Ueda, A. L. Landers, T. Weber, M. H. Prior, A. Belkacem, and R. Dörner, Phys. Rev. A **80**, 032506 (2009).
[37] T. Mizuno, J. Adachi, M. Kazama, M. Stener, P. Decleva, and A. Yagishita, Phys. Rev. Lett. **110**, 043001 (2013).
[38] F. Robicheaux, M. P. Jones, M. Schöffler, T. Jahnke, K. Kreidi, J. Titze, C. Stuck, R. Dörner, A. Belkacem, T. Weber, and A. L. Landers, J. Phys. B **45**, 175001 (2012).
[39] F. Robicheaux, J. Phys. B **45**, 135007 (2012).
[40] X. Wang and F. Robicheaux, Phys. Rev. A **96**, 043409 (2017).
[41] D. Varshalovich, A. Moskalev, and V. Khersonskiĭ, *Quantum Theory of Angular Momentum: Irreducible Tensors, Spherical Harmonics, Vector Coupling Coefficients, 3nj Symbols* (World Scientific, Singapore, 1988).
[42] F. Robicheaux, M. S. Pindzola, and D. R. Plante, Phys. Rev. A **55**, 3573 (1997).
[43] G. Tanner, K. Richter, and J.-M. Rost, Rev. Mod. Phys. **72**, 497 (2000).